UC Davis
UC Davis Previously Published Works

Title
Computations and measurements of the global drag force on a Tension-Leg Platform

Permalink
https://escholarship.org/uc/item/2ns7v0rp

Authors
Dai, SS
Chaplin, JR
Younis, BA
et al.

Publication Date
2021-11-01

DOI
10.1016/j.oceaneng.2021.109710

Peer reviewed

Check for updates

Computations and measurements of the global drag force on a Tension-Leg Platform

S.S. Dai [a,*], J.R. Chaplin [b], B.A. Younis [c], D. Tang [a], T.L. Zhai [a]

[a] *Deep water Engineering Research Center, Harbin Engineering University, Harbin 150001, China*
[b] *Faculty of Engineering and the Environment, University of Southampton, Southampton SO17 1BJ, UK*
[c] *Department of Civil & Environmental Engineering, University of California, Davis, CA 95616, USA*

ARTICLE INFO

ABSTRACT

We present experimental and computational results for the global drag force on a model Tension-Leg Platform (TLP) in uniform current for various values of the Reynolds number in the subcritical regime (Re = 10^4 - 1.06×10^5). The objective of the experiments, which were performed in a towing tank on a representative TLP configuration, was to provide data suitable for validating numerical model predictions. The purpose of the simulations was to determine the extent to which Large-Eddy Simulations (LES), when used as a truly predictive tool, can be relied upon to provide reliable estimates of the total drag force. Thus the simulations were performed only once with no further computations performed in order to bring about closer agreement with the measurements. The dependence of the computed results on the numerical grid was checked using the Grid-Convergence Index (GCI) method applied to results from benchmark flows. These results also served to assess the dependence on the value of the Smagorinsky constant in the model for the sub-grid scale terms. It was found that, at the highest value of Reynolds number considered, the variation between the measured and predicted values of the global drag coefficient was under 10% - a result which is in line with the limitations inherent in both.

1. Introduction

Due to the wide-spread availability of inexpensive and powerful computing platforms, and of associated pre- and post-processing tools, recent years have seen a rapid growth in the use of Computational Fluid Dynamics (CFD) to predict the hydrodynamic loads on offshore structures (Wu et al., 2014; Tan et al., 2013; Younis and Przulj, 2006; Younis and Abrishamchi, 2014; Teigen et al., 1999). However, the accuracy of the numerical predictions, when obtained for realistic offshore structures, has proved difficult to quantify. This is especially true in cases where vortex shedding is present, leading to significant fluctuations in the magnitude of the unsteady hydrodynamic forces on the structure. It is also true in the cases where the unsteady flows generated by the various components of the structure interfere with each other on a very wide range of spatial and temporal scales. In these cases, it is now well established that conventional turbulence closures of the type routinely used in engineering design fail to capture essential features of the resulting flows leading to large uncertainties in the predictions. Moreover, it is often the case that validation of the computed results is done by reference to experimental data from simple, isolated, geometries such as surface-mounted square or circular cylinders. Results obtained in these flows are not particularly useful for quantifying the uncertainty in the prediction of the type of flows that are of interest to the offshore engineering community (Qui et al., 2014). In particular, the ability of the preferred CFD model to capture the effects of the interactions that occur between the various members of the offshore structures, and the massive separation that occurs downstream of them, remains largely untested and it is these interactions that can significantly alter the magnitude of the hydrodynamic forces that apply.

The Large-Eddy Simulation (LES) approach is increasingly thought to be a reliable tool for capturing the large-scale unsteady features of separated flows and hence provide a good estimate of the all important resulting global drag force on the structure. Previous relevant studies include those of Lu et al. (2002) who explored the effects of using non-uniform grids on the simulations, those of Bakker and Oshinowo (2004) and Hartmann et al. (2004) who explored the sensitivity of the simulations to the choice of the sub-grid scale model, and those of Li et al. (2011) and Dai et al. (2014) who assessed its performance in flows where vortex shedding was present. In this paper, we report on experiments conducted for the purpose of obtaining data on the global drag force on a model Tension-Leg Platform, and on the use of these

Nomenclature

A	Projected area (m^2)
A^+	Coefficient in wall damping model
B	Pontoon height (m)
$C_D(t)$	Global drag coefficient
$\overline{C_D}$	Mean drag coefficient
C'_D	Fluctuating drag coefficient
C'_l	Fluctuating lift coefficient
$\overline{C_l}$	Mean lift coefficient
$\overline{C_p}$, C'_p	Static pressure coefficient (mean, fluctuating)
C_s	Smagorinsky constant
C_w	Wavemaking resistance coefficient
D	Column diameter (m)
f_s	Frequency of vortex shedding (Hz)
F_r	Froude number
H	Column height below still water level (m)
Re	Reynolds number
s	Columns center-to-center separation (m)
U_o	Inlet velocity (m/s)
$\overline{U_i}$	Resolved velocity (m/s)
u^+	Velocity in wall coordinates
V	Towing speed (m/s)
W	Pontoon width (m)
y^+	Distance in wall coordinates

Greek symbols

Δ	Spatial filter, grid spacing (m)
Δt^*	Non-dimensional time step
δ_{ij}	Kronecker delta
ν	Kinematic viscosity (m^2/s)
ν_{sgs}	Sub-grid turbulent viscosity (m^2/s)
ρ	Density (kg/m^3)
τ_{ij}	Sub-grid stress (N/m^2)

Table 1
Dimensions of the members of the towing-tank model.

Member	Dimension (m)
Column height (H)	0.32
Column diameter (D)	0.125
Columns separation (s)	0.407
Pontoon width (W)	0.089
Pontoon height (B)	0.089
Draught (H+B)	0.407

extended down to within about 50 mm of the tank floor to provide bottom attachment points for the tethers. At the section where the upstream vertical steel poles penetrated the water surface, they were shrouded as shown to minimize the flow disturbance. Tethered in this way, the model was free to undergo large displacements in surge, sway and yaw. To restrict the latter two degrees of freedom, pins were fitted to the deck of the model to engage loosely between longitudinal guide rails mounted on the carriage. This restricted lateral motion to about ±2 mm, but left the model free to respond in surge. As the bottom of the model was only tethered, the model was subject to small changes in draught and tether angle leading to geometry changes. This will have led to a small change in the flow characteristics and with that to some measure of uncertainty in the measured global drag which we estimate to be of the order of 3%. The layout for the tests is shown in Fig. 1.

The experiments were conducted on a 1 : 70 scale model of the TLP. The model consisted of four pontoons that are square in section, and four circular columns — their dimensions are given in Table 1. All members were made of 3 mm rigid PVC. The columns were terminated at an overall height of 615 mm (202 mm above the still water level) and joined at the top by a single sheet of 5 mm thick plexiglass to provide additional stiffness. The columns and pontoons were sealed to prevent water entry, and the vertical tethers, 2 mm diameter stainless steel cables, entered the base of the columns at their centers and passed upwards through internal thin brass tubes. Adjustable clamps attached to the cables where they emerged at the tops of the columns enabled the model to be set horizontally in the water at the appropriate draught with equal tether tensions in each corner. Careful positioning of the clamps also ensured that the tensions in all four tethers were essentially the same.

The drag forces of the model in steady currents were measured by towing the rig through still water at speeds of up to 0.85 m/s, always in the same direction. The highest Reynolds number (based on column diameter) achieved was thus equal to 1.06×10^5 which, based on Froudian scaling wherein $Re_{model} = Re_{full} \times \lambda^{3/2}$, corresponds to conditions in which the full-scale Reynolds number $Re_{full} = 6.2 \times 10^7$. Between tests the carriage was returned slowly to the starting point, and ample time was then allowed for all detectable motion in the tank to cease. The tests were completed in two series. In the first, the drag-induced rearwards displacement of the model under tow was measured by a non-intrusive optical system (optical displacement transducer) mounted on the carriage above its mid-point to measure the model's displacement against the tension spring. A horizontal tension spring was attached to the model on the upstream side to increase the system's stiffness, and in these conditions the maximum displacement was less than 100 mm. The force and displacement calibrations were carried out in still water by loading the model statically in the horizontal direction, and in processing the measurements, account was taken of the resulting slight changes in draught and tether angles. In the second series of tests, the measurements were repeated without the tension spring and displacement transducer, but with a load cell attached to the rear of the model to measure its drag directly. In these two conditions the natural frequencies of the model in surge were 1.12 Hz and 14.5 Hz respectively. In steady tow cases, the tests were carried out at Froude numbers $Fr = V/\sqrt{gD}$ (where V is the towing speed and D the diameter of the columns) of up to about 0.8, so the estimated drag on the tethers was subtracted from the measured forces.

data in assessing the predictive capabilities of LES in an objective manner; that is by reporting the results obtained from the first application of the model rather than after repeated applications designed to bring about closer agreement with the measurements. The experimental data were obtained from towing-tank tests on a 1 : 70 scale model TLP in steady current at various values of Reynolds number in the sub-critical regime. Attention was confined largely on obtaining measurements of the total drag force, the parameter which is of primary interest in practice. The focus of the assessment was therefore on determination of the degree to which this parameter can be predicted using LES. We expect that the results of this study will provide a useful indication to the offshore engineering community of the predictive capability of LES in practically-relevant flows.

2. Experiments

The tests were carried out in a 55 m flume, 1.71 m wide with water depths of 1.75 m. The flume was equipped at the downstream end with a solid roughened concrete beach with a slope of 1 : 10. Waves generated by the towing of the model reflected from the beach were of no concern however, since each set of measurements was completed before the reflections would have had time to return to the model. Sufficient time was allowed between tests for the water surface to become almost completely still and for the turbulence that was generated in the previous run to be largely dissipated. The flume carriage was fitted with a framework made of 50 mm steel poles, which
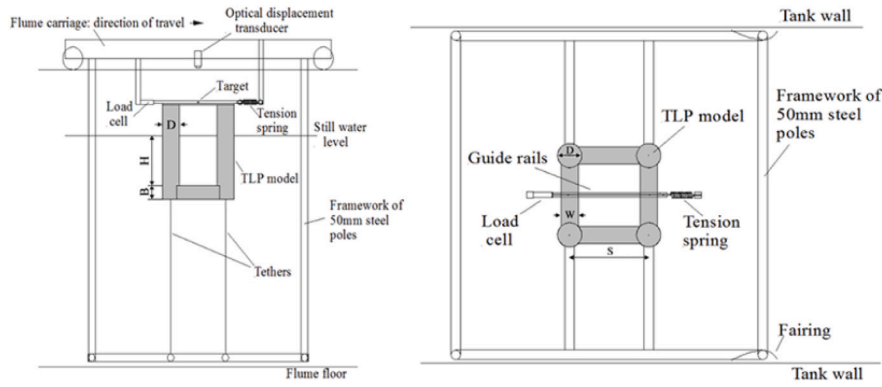
Fig. 1. Elevation (left) and plan (right) views of the model TLP mounted in the towing tank.

In these conditions it is reasonable to expect that the drag would be significantly modified by motion at the free surface around the columns, such as the consequences of a 'bow wave'. To identify this effect, reference is made to the results of a separate set of measurements described in experiment from Chaplin and Teigen (2003), of the loading on a single vertical surface-piercing cylinder in the near surface region. The difference between the measured drag and that obtained by extending up to the still water surface the loading per unit length observed at large submergences provided a measure of the wave-making resistance. This can be represented as a point force at the still water level of magnitude $C_w 1/2\rho V^2 D^2$ where the coefficient C_w is positive when the effects of the free surface lead to an increase to the overall loading. Fig. 2 plotted the curve of C_w against Fr. It can be seen that the wave-making resistance reaches a maximum at $Fr \approx 1$, and that it is negative for Froude numbers in the range 0.4 to 0.64. At $Fr = 0.4$ the measured pressure distribution on a vertical surface-piercing cylinder was almost unchanged up to the still water level, suggesting that in the range $Fr < 0.4$ (covering the actual full-scale conditions for the TLP), the wave-making resistance would be negligible. A polynomial fit to the data, shown in Fig. 2 for $Fr < 1$, was therefore used to provide corrections to the measurements of loading on the model TLP in towing tests in still water at $Fr > 0.4$, on the assumption that the wave-making resistance acted only on the front two columns, the rear columns being substantially shielded from the incident flow.

Fig. 3 plotted the measured drag against the velocity for both series of tests, where the data were shown before and after correction for free surface effects. The result of the corrections is to improve the correlation of the data with straight lines on the graph that correspond to constant drag coefficients ($C_D = F_D/0.5\rho V^2 A$), where A is the global projected area. Overall, a good match is found with $C_D = 1.47$ in the first series of tests, and $C_D = 1.25$ in the second, in which the natural frequency of the model in surge was much higher. However, over a narrow range of velocities from 0.44 m/s to 0.49 m/s ($0.39 < Fr < 0.44$), there was a repeatable and consistent increase in the drag coefficient in the second series of tests, up to a maximum close to that observed in the first, namely 1.47. No other differences were observed in the experiments in this range, except in the output of a wave gauge located on the carriage downstream of the model, and about 0.5 m to the side. The measured curve of drag and velocity for zero incidence is shown in Fig. 3.

In present experimental arrangements the frontal area of the model represented 5.1% of the water cross section, and at similar 'total blockage ratios' in a closed wind tunnel Farell et al. (1977), who measured increases of about 30% in the base suction coefficient on cooling towers but increases in sectional drag coefficients of less than 4%. In measurements of base suction coefficients in open-jet tunnels (in which, rather more like the present case, the flow can expand around the body and its wake) there was almost no change in the pressure distribution at total blockage ratios of up to 10%. It seemed unlikely
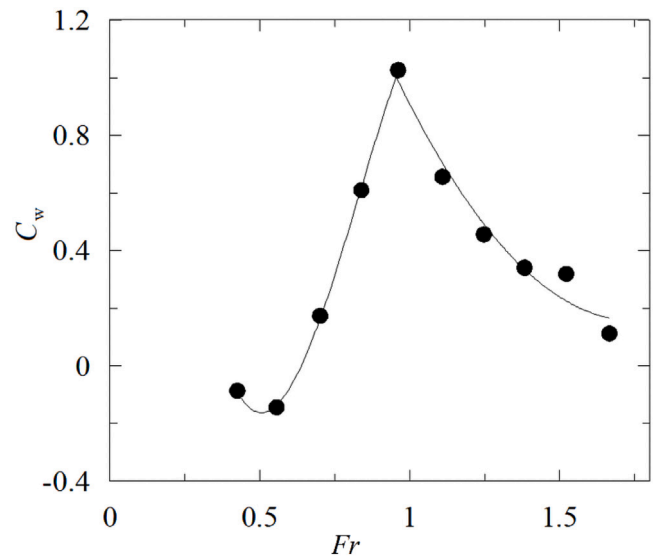

Fig. 2. Wave-making resistance coefficient for a vertical surface-piercing cylinder at constant speed (Chaplin and Teigen, 2003): Lines represent separate polynomial fits for $Fr < 1$ and $Fr > 1$.

therefore that blockage effects in the present case would generate an increase of more than 4% in the drag coefficient, but to investigate the question further some additional measurements were carried out in the first series of tests with false side walls mounted on the carriage to reduce the effective width of the flume from 1.71 m to 1.31 m. Under these conditions the model's drag coefficient was found to increase by 4.4% from 1.47 to 1.53, adding support to the conclusion that the blockage effect at a width of 1.71 m was not more than 4%.

3. Mathematical model

3.1. Governing equations

The methodology underlying the Large-Eddy Simulations approach to modeling turbulent flows is well know (see, for example, Breuer, 1998, 2000; Tremblay et al., 2000). By assuming incompressible flow, the continuity and momentum equations, filtered by using a spatial filter of characteristic length Δ (typically, the grid size), are written using Cartesian tensor notation as:

$$\frac{\partial \overline{U}_i}{\partial x_i} = 0 \tag{1}$$

$$\frac{\partial \overline{U}_i}{\partial t} + \frac{\partial}{\partial x_j}\left(\overline{U}_i \overline{U}_j\right) = -\frac{1}{\rho}\frac{\partial \overline{p}}{\partial x_i} + \frac{\partial}{\partial x_j}\left(\nu \frac{\partial U_i}{\partial x_j}\right) - \frac{1}{\rho}\frac{\partial \tau_{ij}}{\partial x_i} \tag{2}$$
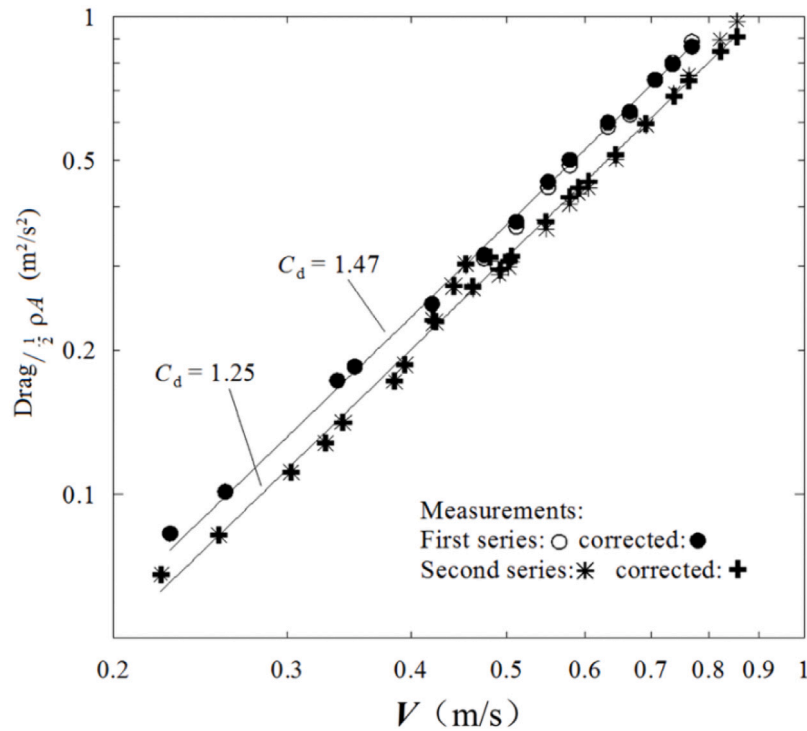
Fig. 3. Global mean drag plotted against velocity:The data are shown with and without corrections for wave-making resistance.

In this study, we use the Smagorinsky (1963) model for the sub-grid scale stresses wherein these correlations are assumed to be linearly proportional to the local, instantaneous, rate of strain:

$$\tau_{ij} = -2\nu_{sgs}\overline{S}_{ij} + \frac{1}{3}\tau_{kk}\delta_{ij} \tag{3}$$

The turbulent eddy viscosity is obtained from

$$\nu_{sgs} = \left(C_S\Delta\right)^2 |\overline{\mathbf{S}}| \tag{4}$$

where $\overline{\mathbf{S}}$ is the invariant for strain rate tensor and Δ is a length scale obtained from:

$$\Delta = \left(\Delta_x\Delta_y\Delta_z\right)^{\frac{1}{3}} \tag{5}$$

where $\Delta_x, \Delta_y, \Delta_z$ are the grid spacings in the x, y, z directions, respectively.

C_s is the Smagorinsky coefficient for which different values have been quoted ranging from 0.1 (Deardoff, 1970) to 0.25 (Lilly, 1966). Several alternatives to the adoption of a constant value for the Smagorinsky coefficient have been proposed and used to varying degrees of success in the prediction of a range of different turbulent flow though, interestingly, rarely in flows, such as the present one, where the random turbulence field is strongly modified by the organized mean-flow periodicity due to vortex shedding (Breuer, 2000). In many cases, these alternative models involve making the coefficient dependent on local or transported quantities and, in some cases, on the computational grid itself. Often, this leads to the generation of negative values for this coefficient, something that produces numerical instabilities. In the present study, we have chosen to adopt the robust constant value approach and to check the sensitivity of the computations to the chosen value by obtaining results for three values for C_s viz. 0.25, 0.10 and 0.0, the last one being included to provide a measure of the importance of the sub-grid terms in determining the overall behavior of the flow.

All computations presented here were performed using the CFX ANSYS 15.0 CFD software. The temporal discretization scheme used was the second-order accurate backward differencing scheme with the time-step size restricted according to the Courant–Friedrichs–Lewy number:

$$CFL = \Delta t \max\left(\frac{|U|}{\Delta x} + \frac{|V|}{\Delta y} + \frac{|W|}{\Delta z}\right) \tag{6}$$

CFL was set equal to 0.6 yielding a maximum non-dimensional time-step value of Δt^* $(=\Delta t.U_o/D)$ of 0.0192 which was found to yield time-step independent solutions.

The Smagorinsky model with a constant C_S tends to overpredict the viscosity in close proximity to the wall and hence, following the usual practice, we use van Driest's damping function to bring about the correct asymptotic behavior:

$$\nu_{sgs} = \left(C_S\Delta\right)^2 |\overline{\mathbf{S}}|\left(1 - e^{-y^+/A^+}\right) \tag{7}$$

where $y^+ = \frac{u_\tau y}{\nu}$ is the non-dimensional wall distance and $A^+ = 26$.

Concerning the spatial discretization, the Laplacian terms were discretized using the Gauss linear corrected scheme, while the convective fluxes were approximated using the Gauss limited linear V integral discrete lattice, both being second-order accurate. The governing equations were solved iteratively with the SIMPLE algorithm (Semi-Implicit Method for Pressure-Linked Equations) from Patankar and Spalding (1972) used to couple the solution of the continuity and momentum equations. The convergence criterion for the iterative solution procedure at each time step was set to be when the normalized residuals fell below 10^{-6}.

The boundary conditions were as follows: at inlet, a uniform velocity was prescribed according to the experimental Reynolds numbers. At the exit, fully-developed flow conditions were assumed so that the streamwise gradients of all dependent variables were set to zero. All remaining boundaries were treated as planes of symmetry. The TLP surfaces were assumed to be smooth with the no-slip boundary condition applied. The calculations were performed on the graphics workstation, which has 72 cores in parallel with 128 GB of RAM.

4. Results and discussion

To validate the computer model, simulations were first performed for two representative cases that share many of the features present
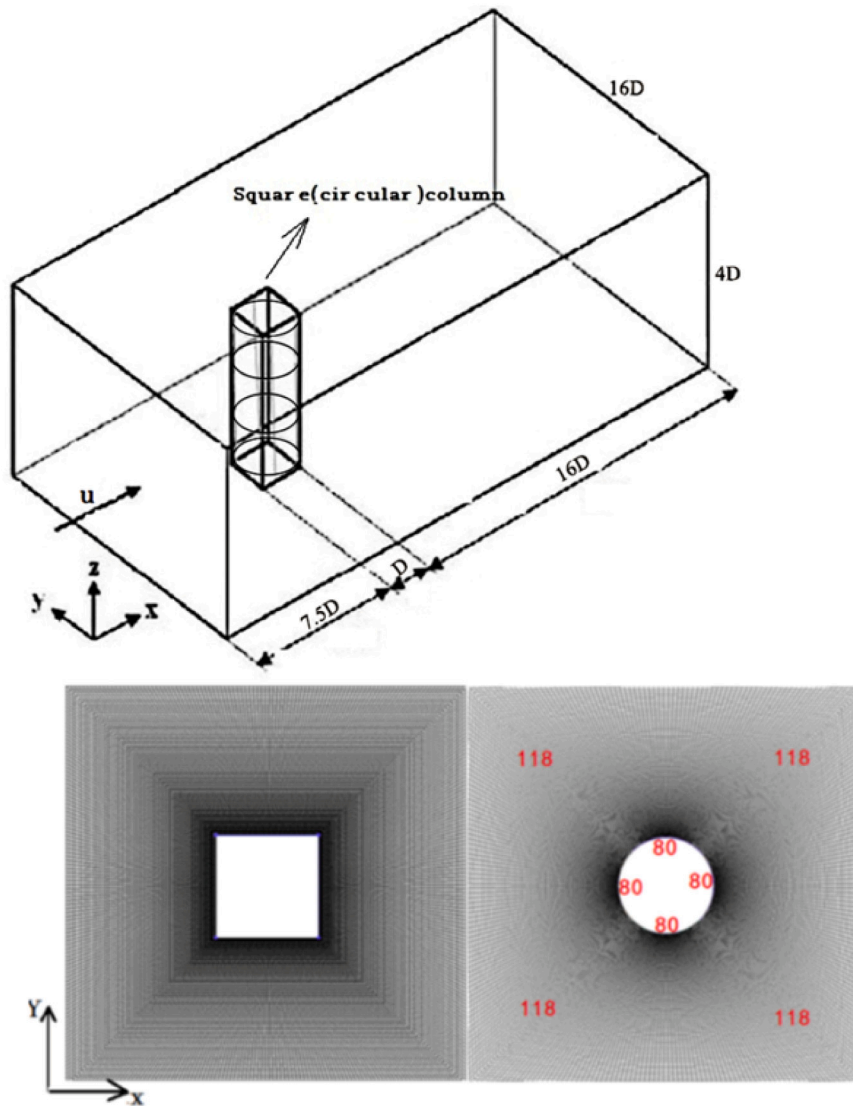
Fig. 4. Geometry, computational domain and dimensions.

in the TLP case, namely the three-dimensional flows around a circular column and a square-sectioned one. These flows are generally considered to be important test cases for the validation of computer models for flows with vortex shedding. They have, moreover, been the subject of numerous experimental studies that have yielded data suitable for model validation. The columns geometries, and the extent of the computational domain are shown in Fig. 4. For both the circular and the square-sectioned columns, the cross-sectional dimension was D, and the height was 4D. The inlet to the computational domain was located at distance 8D from the center of the columns while the outlet was placed at distance of 16D from the downstream face. The overall width of the domain was 16D. The incident flow was aligned with the x-axis. To ensure adequate resolution of the flow, the computational grids used were constructed in a number of separate non matching blocks based on O topology using the ICEM-CFD software. The grid lines were non-uniformly distributed with the highest concentration of cells being adjacent to the column where the velocity variations were steepest. For the finest mesh used, the total number of nodes in direct contact with cylinder was 320 with a total of 590,804 active cells being used to resolve the flow field (Fig. 4). The boundary conditions are same as the mentioned above.

To quantify the influence of the sub-grid scale model parameter C_s, predictions were obtained for three different values spanning the range of values used in previous studies. Computed predictions of the surface pressure distribution for both the circular and square columns are compared with experiments in Fig. 5. The Reynolds number for the circular column was $Re = 4.4 \times 10^4$ and for the square column 2×10^4. For the circular column, the experimental results were those of Cantwell and Coles (1983) and Qiu et al. (2014), both of which were for Reynolds number in the sub-critical regime. it can be clearly seen from Fig. 5 that the peak of the mean wall-pressure coefficient ($\overline{C_p}$) is coincident with the experimental value when $C_s = 0$ up to a turning angle $\theta = 60°$ thereafter appearing to slightly underpredict the data. For $C_s = 0.25$, the predictions show greater departures from the data especially with regards to the peak negative value. A similar behavior is obtained with $C_s = 0.1$ albeit with smaller negative peak. For the case of the square column, the predicted $\overline{C_p}$ vs. θ curves show much greater dependence on the value of C_s with the value 0.1 yielding the closest agreement with the experimental data.

The effects of C_s on the distribution of the fluctuating pressure (C_p') is examined next. For the case of the circular column, the results at the mid-height section for the three values of C_s are presented in Fig. 6. It is evident there that the predictions are broadly in accord with the measurements considering the scatter observed in the latter. Similar trends are observed for the square column. With $C_s = 0.1$, the distribution of C_p' is in very close agreement with the experimental data of Bearman and Obasaju (1982) for values of θ less than 90°.
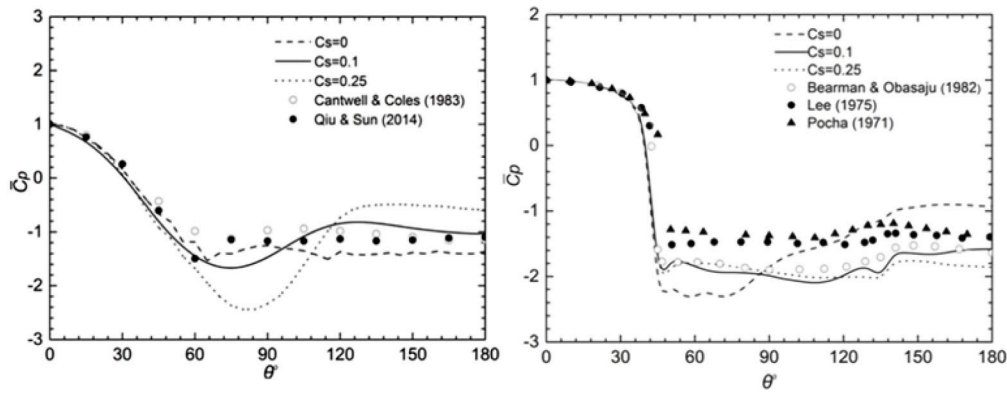
Fig. 5. Predicted and measured mean wall-pressure coefficient at mid-sections of circular and square columns with different C_s: (Left) Circular column ○ Cantwell and Coles ($Re = 6.9 \times 10^4$), • Qiu et al. ($Re = 1.6 \times 10^5$); (Right) square column: ○ Bearman and Obasaju ($Re = 2 \times 10^4$), • Lee ($Re = 1.76 \times 10^5$), ▲ Pocha ($Re = 9.2 \times 10^4$.).
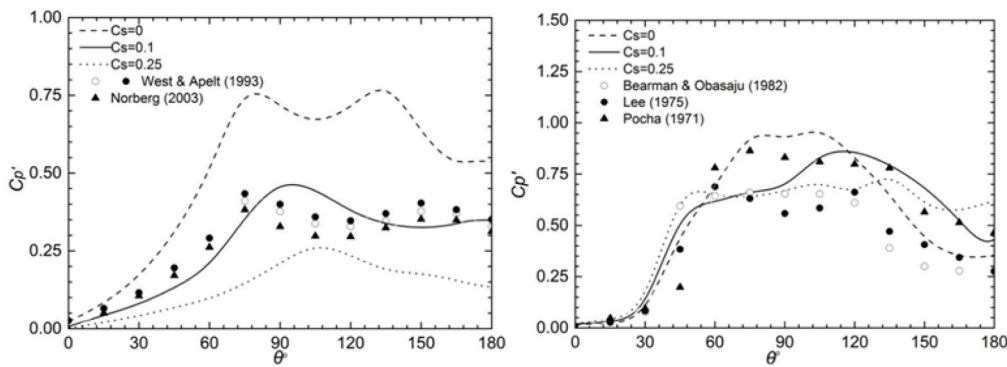

Fig. 6. Predicted and measured fluctuating wall-pressure coefficients distribution at the middle section of 3D circular and square columns with different C_s: (Left) Circular column ○ • West and Apelt ($Re = 4.4 \times 10^4, 6.6 \times 10^4$), ▲ Norberg ($Re = 6.1 \times 10^4$) (Right) square column ○ Bearman and Obasaju ($Re = 2.0 \times 10^4$), • Lee ($Re = 1.76 \times 10^5$), ▲ Pocha ($Re = 9.2 \times 10^4$).
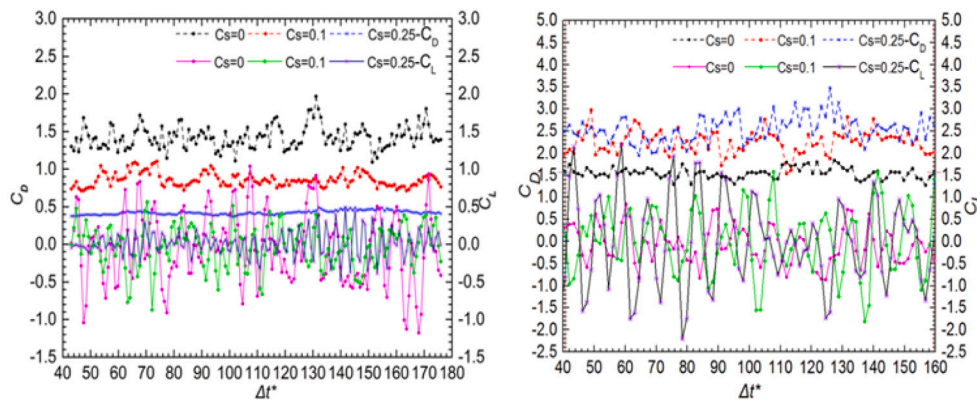

Fig. 7. Predicted transient force coefficients for circular and square columns with different C_s values.

A quantitative assessment of the sensitivity of the predicted results on C_s is obtained from comparison between the predicted and measured non-dimensional force parameters that characterize this flow. This is shown in Tables 2 and 3. Fig. 7 presents the time history of force parameters for circular and square columns. It is clear from this table that the numerical results are better accord with the measurements as C_s is equal to 0.1.

Attention is turned next to the computation of the flow around the model Tension-Leg Platform described above. The extent of the computational domain is shown in Fig. 8. All dimensions are referenced to the column diameter (D). Except for the inlet, the other three sides of the domain are not shown for clarity. The actual domain size is 50D, 16D, 9.76D. The center of the front cylinder was located at $x = 6.5D$

and $y = 1.6D$. The distance between the centers of the two cylinders is $s/D = 3.257$. These dimensions were found to be sufficient to ensure that simulations are not influenced by the boundary conditions or by blockage effects (Dai et al., 2015; Younis and Przulj, 2006; Farell et al., 1977). To ensure adequate resolution of the flow, the computational grids used were constructed in the form of a non-uniformly structured hexahedral mesh that was generated by ICEM-CFD. Fig. 8 shows the details of the surface nodes distribution by both isometric and top views. The boundary conditions used in the computations were unchanged from before.

In order to estimate the discretization errors, the Grid Convergence Index (GCI) method was used (Celik et al., 2008). This method involves performing computations on three different grids and then
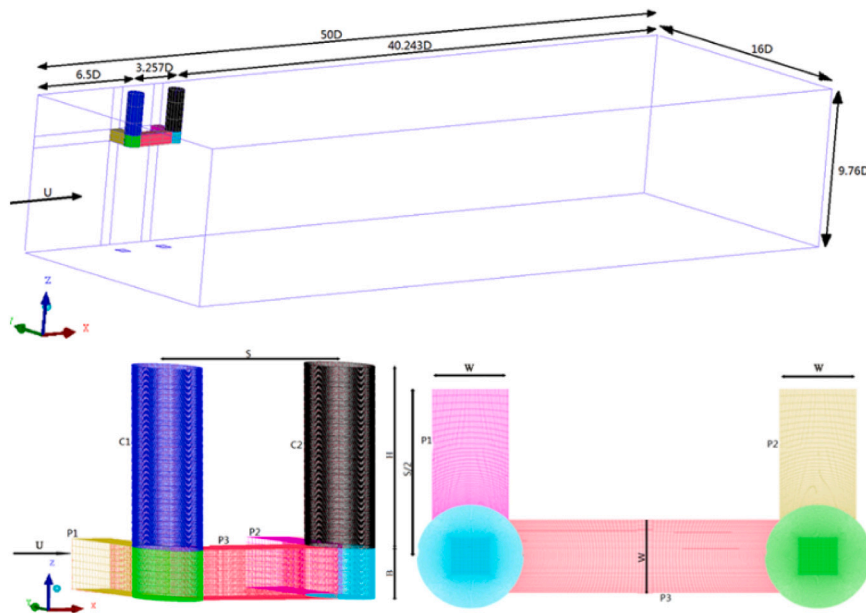
Fig. 8. Model geometry and grid distribution.

Table 2

Predicted and measured bulk parameters for circular column ($Re = 4.4 \times 10^4$). (a) DuarteRibeiro (1992), $Re = 4.0 \times 10^4 - 3.5 \times 10^5$, (b) Ma et al. (2019), $Re = 5.0 \times 10^4 - 4.5 \times 10^5$, (c) West and Apelt (1993), $Re = 4.4 \times 10^4, 6.6 \times 10^4$, (d) Humphreys (1960), $Re = 3.0 \times 10^4 - 5.7 \times 10^5$, (e) Ferguson and Parkinson (1967), $Re = (1.5–4.0) \times 10^4$, (f) Protos et al., $Re = 4.5 \times 10^4$, (g) Nishimura and Taniike (2001), $Re = 6.1 \times 10^4$.

C_s	C_D	C'_D	C'_L	St
0	1.423	0.153	0.478	0.174
0.1	0.950	0.106	0.275	0.220
0.25	0.422	0.027	0.173	0.303
Measurements	0.90–1.15 (a)	0.137 (c)	0.20–0.50 (d)	0.196 (b)
-ditto-	1.115 (b)		0.22–0.32 (e)	0.202 (g)
-ditto-			0.28 (f)	

Table 3

Predicted and measured bulk parameters for square column ($Re = 2.0 \times 10^4$). (a) Tamura and Miyagi (1999), $Re = 3.0 \times 10^4$, (b) Carassale et al. (2014), $Re = 3.7 \times 10^4$, (c) Younis and Przulj (2006), $Re = 2.0 \times 10^4$, (d) Bearman and Trueman (1972), $Re = (2.0–7.0) \times 10^4$, (e) Bearman and Obasaju (1982), $Re = 5.8 \times 10^3 - 3.2 \times 10^4$.

C_s	C_D	C'_D	C'_L	St
0	1.551	0.123	0.414	0.106
0.1	2.249	0.262	0.901	0.112
0.25	2.547	0.291	1.008	0.125
Measurements	2.10 (a)		1.05 (a)	0.123 (d)
-ditto-	2.06 (b)		1.02 (b)	0.130 (e)
-ditto-	2.16–2.28 (c)	0.18–0.23 (c)	1.1–1.4 (c)	

using the results to estimate the actual order of accuracy of the discretization method, and the theoretically-implied asymptotic value of

a pre-selected target parameter. The results of this assessment are presented in Table 4. The grids used in this assessment consisted of $2,155,659$, $2,624,318$ and $2,983,980$ active cells. The number of cells that were in direct contact with the column surface in each case was 240, 320 and 400, respectively. The target parameters chosen for this purpose were the global and individual drag force coefficients for the TLP. The analysis was performed for the case of $Re = 5 \times 10^4$. The extrapolated values (Φ^{21}_{ext}) and fine-grid convergence index (GCI^{21}_{fine}) were calculated according to global cell size or local cell size (see Table 4). Based on the outcome of applying the GCI method, the estimated maximum discretization error was found to occur in the calculation of the mean drag coefficient for column 1 where its value there was 3.53%.

A series of computations were performed on TLP at different Reynolds number. The principal features of the flow are the occurrence of vortex shedding from each member, and the large modification to the flow field that arises when vortices shed from upstream members interact with those shed from the downstream ones. To illustrate this complex flow phenomena, the predicted pressure and eddy viscosity contour at the middle height of the columns are shown in Fig. 9. The phase indicated on the plots is that of the lift cycle on the forward cylinder with the phase angle being 0 when $C_l = 0$. As shown in Fig. 9, the highest pressure levels occur at the stagnation points at the front column, while lower pressure occurs at the stagnation point of the aft column. This is caused by the shielding effect from the front column. When the phase angle is equal to $\pi/2$, the pressure at the upper part of the separation zone is significantly lower than that in the lower part for each of column and this produces the highest lift forces on

Table 4

The GCI method estimates of the discretization errors in the TLP calculations.

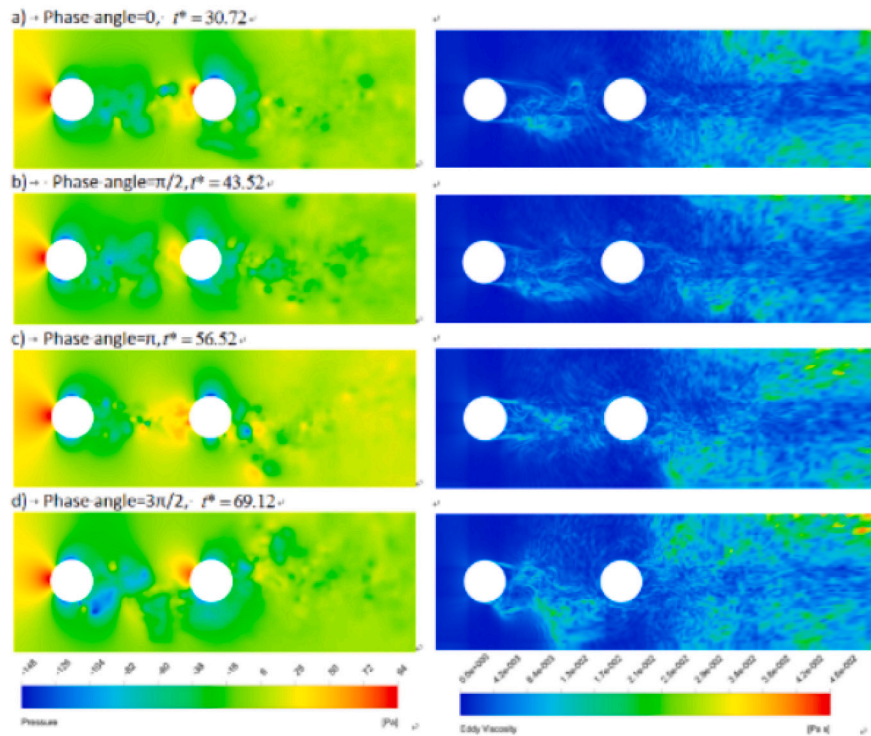| Variables/coefficients	$\phi = \overline{C_{D\,Global}}$	$\phi = \overline{C_{D\,Col\ 1}}$	$\phi = \overline{C_{D\,Col\ 2}}$	$\phi = \overline{C_{D\,Pont\ 1}}$	$\phi = \overline{C_{D\,Pont\ 2}}$
$N_1,\ N_2,\ N_3$	2,983,980 (400); 2,624,318 (320); 2,155,659 (240)				
γ_{21}	1.044				
γ_{32}	1.068				
ϕ_1	1.346	0.623	0.511	1.600	0.455
ϕ_2	1.347	0.645	0.519	1.574	0.454
ϕ_3	1.349	0.649	0.559	1.545	0.447
p	4.880	86.11	21.01	10.45	26.73
ϕ^{21}_{ext}	1.342	0.622	0.506	1.646	0.455
e^{21}_a	0.07%	3.53%	1.60%	1.63%	0.22%
GCI^{21}_{fine}	0.4%	0.11%	1.3%	3.6%	0.13%

Fig. 9. Pressure and eddy viscosity contours at mid-height of TLP column.

both columns. At the phase angle of π, with the continued increase of the pressure at the stagnation point of both columns, the drag forces increase on both columns quite substantially. As can be seen in Fig. 9, the distribution of pressure at the upper and lower part of separation zone is opposite to the phase angle of $\pi/2$, therefore the lift force reaches minimum value, while the drag on the surface of front column is larger than the aft columns. The contours of turbulent viscosity are plotted in Fig. 9. It is seen that high eddy viscosity does not occur at the stagnation point, while higher eddy viscosity is generated in the interval gap of columns and wake of after column, as well as it develops gradually from initial symmetry at phase angle 0 to asymmetry at phase angle $\pi/2$ and $3\pi/2$. Meanwhile, the eddy viscosity reaches maximum at those two phases.

The global drag coefficients (C_D) for the TLP are calculated based on the force coefficients for each TLP member and its projected area. The mean and root-mean-square values of the global drag coefficients $(\overline{C_D}, C_{D\ rms})$ are obtained based on time histories of the global force coefficients:

$$C_D(t) = \frac{\Sigma C_{d_i}(t) \times A_i}{\Sigma A_i} \tag{8}$$

Here, A_i is projected area of every component and C_{d_i} are drag and lift coefficients of the loads acting on the ith member of the TLP.

The global drag coefficient on TLP is calculated by using Eq. (8). Fig. 10 (left) presents the variation of the TLP global mean drag coefficient with Re. Also shown there are the experimental measurements that are available in the range $10^4 < Re < 1.5 \times 10^5$. It is clear that the Reynolds number has little influence on the variation of $\overline{C_D}$ in the subcritical regime. Although the measured $\overline{C_D}$ showed a slight fluctuation near the predicted values, the reported values of $\overline{C_D}$ are close to the experimental values, which is in the range of 1.20–1.35. It should be noted that the measured value $\overline{C_D}$ at $Re = 5 \times 10^5$ appears to be out of line with the general trend. Fig. 10 (right) presents the global fluctuating drag coefficients $(C_{D\ rms})$ on the TLP for different Reynolds number. In contrast to the global mean drag, the $C_{D\ rms}$ values are very small, being less than 10% of the global mean drag coefficients. $C_{D\ rms}$ values fluctuates slightly near 0.09 for different Reynolds number.

Fig. 11 presents the contribution that the drag on each member of the TLP makes to the global drag. The predicted $\overline{C_D}$ value for the front column (C1) is about 0.66 when $Re < 1.125 \times 10^5$, thereafter rising rapidly to about 0.75. These values are nearly 1.5 times the value for the aft column (C2), and approximate half of $\overline{C_D}$ the global value for the TLP. The comparison of the predicted values for the pontoons obtained by LES method is shown in Fig. 11. Due to the effect of the change in cross-sectional shape from circular to rectangular, the $\overline{C_D}$ values on the front pontoon (P1) turn out to be the largest, reaching a value of about 1.6. The trend of $\overline{C_D}$ with Re is close to a horizontal line. The $\overline{C_D}$ value on aft pontoon (P2) is about 0.35, i.e. about 20% of the value for the front pontoon. The variation of $\overline{C_D}$ with Re is also quite modest, which is similar to the behavior seen for the front pontoon.

Fig. 12 presents a comparison between the fluctuating drag coefficients $(C_{d\ rms})$ on columns (C1, C2) and pontoons (P1, P2), and shows their variation with Reynolds number. It is clearly apparent that the trend in the values of $C_{d\ rms}$ for each members is opposite to the trends observed for $\overline{C_d}$. Thus due to the occurrence of vortex shedding and the development of well-defined oscillating wake (Fig. 9), the $C_{d\ rms}$ values on the downstream structures are larger than those on the upstream members. With increase of Re, $C_{d\ rms}$ value on aft column (C2) tends to a stable value of 0.085 after a steep drop, while $C_{d\ rms}$ value on front column (C1) tends to a stable value of 0.074 after a slow increase. The $C_{d\ rms}$ values on pontoons (P1, P2) are much larger than that those on the columns, with the value on the aft pontoon being more than twice that of the aft column.

5. Concluding remarks

The flow and the hydrodynamic loads on a model Tension Leg Platform have been investigated by experiments and Large-Eddy Simulations. The aim was to assess the ability of LES to predict the global drag force on this structure. Assessment of the computational model was first carried out for the benchmark problems of flow around three dimensional circular and square columns in the subcritical regime. The influence of Smagorinsky's constant on numerical results was assessed
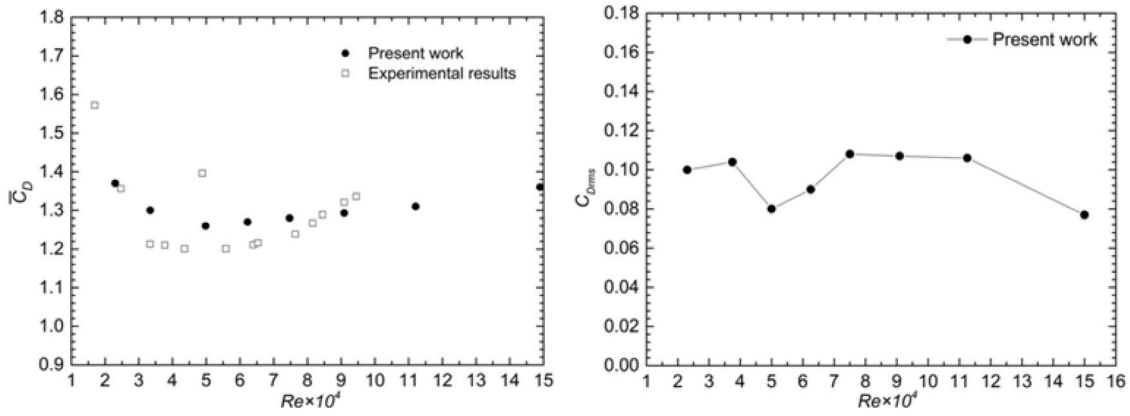
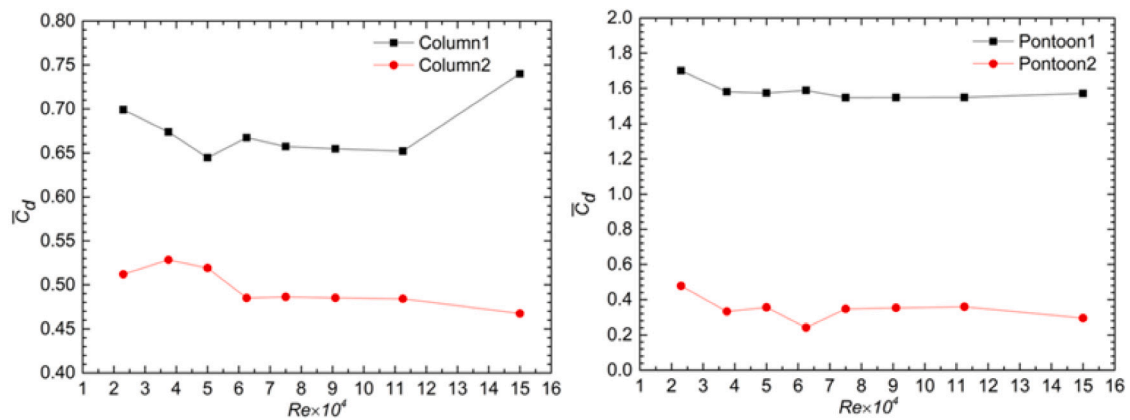**Fig. 10.** Predicted and measured variation of TLP global drag coefficient with Reynolds number.

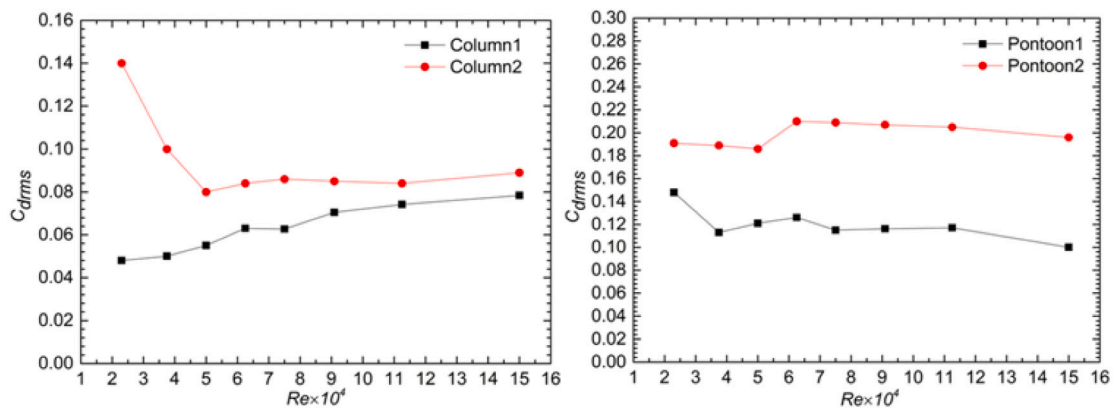**Fig. 11.** Comparison of time-averaged drag coefficients for columns and pontoons.

Fig. 12. Comparison of fluctuating drag coefficients on columns and pontoons.

by analyzing pressure distribution and force coefficients at the middle section of columns. It was found that the LES method, when used in a truly predictive mode i.e. without attempts being made to successively bring about closer agreement with the measurements, can predict the global mean drag coefficient to within about 10% of the measured values. It was also found that the mean drag coefficients of front column and pontoon make the greatest contribution to the global mean drag coefficient. The mean drag coefficient of the aft column was found to be smaller than that of aft pontoon. The fluctuating drag coefficients for every member of TLP are small and show the fluctuating drag

coefficients for the aft members are larger than for the front members due to the effects of vortex shedding from the latter.

CRediT authorship contribution statement

S.S. Dai: Directed the computations, Contributed to writing the paper . **J.R. Chaplin:** Designed and directed the experiments, Contributed to writing the paper. **B.A. Younis:** Participated in the experimental and computational programs, Contributed to writing the paper. **D. Tang:** Contributed to the performance of the computations. **T.L. Zhai:** Contributed to the performance of the computations.

Declaration of competing interest

The authors declare that they have no known competing financial interests or personal relationships that could have appeared to influence the work reported in this paper.

Acknowledgments

References

Bakker, A., Oshinowo, L.M., 2004. Modelling of turbulence in stirred vessels using large eddy simulation. Chem. Eng. Res. 82, 1169–1178.

Bearman, P.W., Obasaju, E.D., 1982. An experimental study of pressure fluctuations on fixed and oscillating square-section cylinders. J. Fluid Mech. 119, 297–321.

Bearman, P.W., Trueman, D.M., 1972. An investigation of the flow around rectangular cylinders. Aeronaut. Q. 23 (3), 229–237.

Breuer, M., 1998. Large eddy simulation of the subcritical flow past a circular cylinder: Numerical and modeling aspects. Internat. J. Numer. Methods Fluids 28, 1280–1302.

Breuer, M., 2000. A challenging case for large eddy simulation of high Reynolds number circular cylinder flow. Int. J. Heat Fluid Flow 21, 648–654.

Cantwell, B., Coles, D., 1983. An experimental study of entrainment and transport in the turbulent near wake of a circular cylinder. J. Fluid Mech. 136, 321–374.

Carassale, L., Freda, A., Marre-Brunenghi, M., 2014. Experimental investigation on the aerodynamic behavior of square cylinders with rounded corners. J. Fluids Struct. 44, 195–204.

Celik, I.B., Ghia, U., Roache, P.J., Freitas, C.J., Coleman, H., Read, P.E., 2008. Procedure for estimation and reporting of uncertainty due to discretization in CFD applications. J. Fluids Eng. 130 (7), 078001-1–078001-4.

Chaplin, J.R., Teigen, P., 2003. Steady flow past a vertical surface-piercing circular cylinder. J. Fluids Struct. 18 (3), 271–285.

Dai, S., Younis, B.A., Sun, L.P., 2014. Large-Eddy Simulation of cavitation in a square surface cavity. Appl. Math. Model. 38, 5665–5683.

Dai, S., Younis, B.A., Sun, L.P., 2015. OpenFOAM predictions of hydrodynamics loads on full-scale TLP. Ocean Eng. 102, 162–173.

Deardoff, J.W., 1970. A numerical study of three-dimensional turbulent channel flow at Reynolds number. J. Fluid Mech. 41, 453–480.

DuarteRibeiro, J., 1992. Fluctuating lift and its spanwise correlation on a circular cylinder in a smooth and in a turbulent flow: A critical review. J. Wind Eng. Ind. Aerodyn. 40, 79–198.

Farell, C., Carrasquel, S., Guven, O., Patel, V.C., 1977. Effect of wind-tunnel walls in the flow past circular cylinder and cooling tower models. Trans. ASME, J. Fluids Eng. 99 (3), 470–479.

Ferguson, N., Parkinson, G.V., 1967. Surface and wake flow phenomena of the vortex-excited oscillation of a circular cylinder. Trans. ASME, J. Eng. Ind. 89, 831–838.

Hartmann, H., Derksen, J.J., Montavon, C., 2004. Assessment of large eddy simulation and RANS stirred tank simulations by means of LDA. Chem. Eng. 59, 2419–2432.

Humphreys, J.S., 1960. On a circular cylinder in a steady wind at transition Reynolds numbers. J. Fluid Mech. 9, 603–612.

Lee, B.E., 1975. The effect of turbulence on the surface pressure field of a square prism. J. Fluid Mech. 69 (2), 263–282.

Li, Z.P., Bao, Y.Y., Gao, Z.M., 2011. PIV experiments and large eddy simulations of single-loop flow fields in Rushton turbine stirred tank. Chem. Eng. Sci. 66, 1219–1231.

Lilly, D.K., 1966. On the Application of the Eddy-Viscosity Concept in the Inertial Sub-Range of Turbulence. Tech. Rep. 123, NCAR.

Lu, Z.Y., Liao, Y., Qian, D.Y., 2002. Large eddy simulation of a stirred tank using the lattice Boltzmann method on a non-uniform grid. J. Comput. Phys. 181, 675–704.

Ma, W., Liu, Q., Macdonald, J.H.G., Yan, X., Zheng, Y., 2019. The effect of surface roughness on aerodynamic forces and vibrations for a circular cylinder in the critical Reynolds number range. J. Wind Eng. Ind. Aerodyn. 187, 61–72.

Nishimura, H., Taniike, Y., 2001. Aerodynamic characteristics of fluctuating forces on a circular cylinder. J. Wind Eng. Ind. Aerodyn. 89, 713–723.

Norberg, C., 2003. Fluctuating lift on a circular cylinder: Review and new measurements. J. Fluids Struct. 17, 57–96.

Patankar, S.V., Spalding, D.B., 1972. A calculation procedure for heat, mass and momentum transfer in three-dimensional parabolic flows. Int. J. Heat Mass Transfer 15 (10), 1787–1806.

Pocha, J.J., 1971. On Unsteady Flow Past Cylinders of Square Cross-Section (Ph.D. Thesis). Department of Aeronautics, Queen Mary College, London.

Protos, A., Goldschmidt, V.W., Toebes, G.H., 1968. Hydroelastic forces on bluff cylinders. J. Fluids Eng. 90 (3), 378–386.

Qiu, Y., Sun, Y., Wu, Y., Tamura, Y., 2014. Effects of splitter plates and Reynolds number on the aerodynamic loads acting on a circular cylinder. J. Wind Eng. Ind. Aerodyn. 127, 40–50.

Qui, W., Junior, J.S., Lee, D., Lie, H., Magarovskii, V., Mikami, T., Rousset, J.-M., Sphaier, S., Tao, L., Wang, X., 2014. Uncertainties related to predictions of loads and responses for ocean and offshore structures. Ocean Eng. 86, 58–67.

Smagorinsky, J., 1963. General circulation experiments with the primitive equations. Mon. Weather Rev. 91, 99–164.

Tamura, T., Miyagi, T., 1999. The effect of turbulence on aerodynamic forces on a square cylinder with various corner shapes. J. Wind Eng. Ind. Aerodyn. 83 (1–3), 135–145.

Tan, J.H.C., Magee, A., Kim, J.W., Teng, Y.J., Zakni, N.A., 2013. CFD simulation for vortex induced motions of a multi-column floating platform. In: Proc. ASME 32nd Int. Conf. on Ocean, Offshore and Arctic Engineering. June 9–14 2013, Nantes. Paper number OMAE2013-11117.

Teigen, P., Przulj, V.P., Younis, B.A., 1999. A CFD investigation into the effects of current incidence on the hydrodynamic loading on a deepwater TLP. J. Offshore Mech. Arctic Eng. 121 (2), 109–115.

Tremblay, F., Manhart, M., Friedrich, R., 2000. DNS of flow around the circular cylinder at subcritical Reynolds number with Cartesian grids. In: Proceedings of the 8th European Turbulence Conference. EUROMECH, Barcelona, Spain, pp. 659–662.

West, G.S., Apelt, C.J., 1993. Measurements of fluctuating pressures and forces on a circular cylinder in the Reynolds number range 1.0×10^4 to 2.5×10^5. J. Fluids Struct. 7, 227–244.

Wu, G., Jang, H., Kim, J.W., Ma, W., Wu, M.-C., O'Sullivan, J., 2014. Benchmark of CFD modelling of TLP free motion in extreme wave event. In: Proc. ASME 33rd Int. Conf. on Ocean, Offshore and Arctic Engineering. June 8–13 2014, San Francisco. Paper number OMAE2014-24658.

Younis, B.A., Abrishamchi, A., 2014. Three-dimensional turbulent vortex shedding from a surface-mounted square cylinder: Predictions with Large-Eddy Simulations and URANS. Trans. ASME, J. Fluids Eng. 136 (6), 060907.

Younis, B.A., Przulj, V.P., 2006. Prediction of hydrodynamic loading on a mini TLP with free surface effects. Ocean Eng. 33 (2), 181–204.